
Contents

6	Characterizing the CNM in M82	1
6.1	Introduction	2
6.2	Observations	3
6.3	Data Reduction	5
6.4	Extracting and Stacking the CRRLs	7
6.5	Results	8
6.6	Discussion	14
6.7	Conclusions	15
	Bibliography	18

List of Figures

Chapter 6	1
6.1 Stacked CRRL spectrum from spectral windows 1 and 2	9
6.2 Confidence intervals for CRRL optical depths for a grid of T_e and n_e	12
6.3 Integrated optical depths with best-fit models	13

List of Tables

Chapter 6	1
6.1 Observational summary of the data taken with the JVL A.	4
6.2 Details of spectral windows and flagging percentages	6

Characterizing the Cold Neutral Medium in M82 with Carbon Radio Recombination Lines

“All you really need to know for the moment is that the universe is a lot more complicated than you might think, even if you start from a position of thinking it’s pretty damn complicated in the first place.”

–Douglas Adams–

We present observations of carbon radio recombination lines (CRRLs) from the nearby starbursting galaxy M82, with the first use of the P band of the Karl G. Jansky Very Large Array for spectroscopy. The aim of this study is to use these and previous CRRL observations of M82 to constrain the electron temperature T_e and density n_e of the cold neutral medium (CNM) in M82. When stacking only 10 of the available 50+ α -transitions ($\Delta n = 1$) we find a lower limit to the emission integrated optical depth of -100Hz . By combining this limit with previous CRRL detections in M82 and comparing with detailed theoretical models of low-frequency CRRLs, we determine $T_e = 95^{+105}_{-85}\text{K}$ and $n_e = 0.030 \pm 0.005\text{cm}^{-3}$. These values are similar to Galactic CRRL results and consistent with an origin in the CNM. Using previously measured H I column densities and a path length of $L = 340\text{pc}$ corresponding to previous measurements of the H I distribution, we estimate $\text{C II}/\text{H I} \lesssim 1.1 \times 10^{-3}$.

Zoutendijk, S. L., Morabito, L. K., Toribio, M. C., Oonk, J. B. R., Salgado, F.,
Salas, P., Röttgering, H. J. A., Tielens, A. G. G. M., et al.

In preparation

6.1 Introduction

The interstellar medium (ISM) is the repository of stellar ejecta and the birthsite of new stars and, hence, a vital factor in the evolution of galaxies over cosmic time. Cold, diffuse H I clouds are a key component of the ISM, but so far this phase has eluded detailed studies, because the main tracer, the 21-cm line, does not constrain basic physical information of the gas (e.g., temperature, density) well. With the advent of new and upgraded telescopes it is now possible to study this component of the ISM through low-frequency ($\lesssim 500$ MHz) carbon and hydrogen radio recombination lines (RRLs), which do provide a unique, sensitive probe of the physical conditions in cold, neutral clouds. Recently, Morabito et al. (2014) used the Low Frequency Array (LOFAR; van Haarlem et al., 2013) to detect carbon radio recombination lines (CRRLs) in absorption in the nearby starburst galaxy M82. The authors stacked 22 α -transitions ($\Delta n = 1$) in the frequency range 48 to 64 MHz ($n = 488$ – 508) to achieve an 8.5σ detection. The observed line profile had a peak line-to-continuum intensity of 3×10^{-3} , a FWHM of 31 km s^{-1} , and was centred on a velocity of 211 km s^{-1} with respect to LSR.

The velocity of the observed CRRL absorption feature indicates that it is associated with the nuclear starburst in M82. This compact region spans about 60 arcsec (approximately 1000 pc), and hosts a wide range of ISM phases. Observations of disrupted H I within the disk shows that the neutral gas is more concentrated in the nuclear region (Yun et al., 1993), where a high concentration of molecular gas is also seen (Lo et al., 1987). Observations of dense gas tracers associated with star formation indicate the presence of a rotating ring of lower density molecular gas (Kepley et al., 2014). The nuclear region is also studied with compact, bright supernova remnants (SNRs; e.g., Muxlow et al., 1994; Fenech et al., 2010), and H II regions (e.g., McDonald et al., 2002; Gandhi et al., 2011). Free-free absorption by ionised gas is also evident, seen in the spectral turnover of the SNRs (Wills et al., 1997) and the overall spectrum (Adebahr et al., 2013). The CRRLs trace a low electron density, low-temperature neutral gas component in this complex environment, but there are two main questions that a single LOFAR LBA detection cannot answer. First, by comparing the integrated optical depths and line widths of RRLs with detailed physical models, we can determine information on the physical properties of the gas, such as electron temperature and density (e.g., Salgado et al., in preparation; Ponomarev & Sorochenko, 1992; Walmsley & Watson, 1982; Brocklehurst & Seaton, 1972). The values of these observables depend sensitively on temperature and density as a function of quantum number (or equivalently frequency). Therefore, to determine these physical properties (T_e , n_e), it is crucial to observe the

CRRLs over a range of frequencies from about 50 to 500 MHz. Second, although Morabito et al. (2014) concluded that the CRRLs were likely associated with the nuclear region, M82 was unresolved in the LOFAR images. In order to understand the role of the cold neutral medium in the life cycle of the ISM in M82, it is important to establish firmly whether the CRRLs do originate in the nuclear region.

The Karl G. Jansky Very Large Array (JVLA; Perley et al., 2011) is the ideal instrument to answer these two questions. The P-band frequency range we use (248–480 MHz) covers 62 CRRL α -transitions. Even with flagging due to radio frequency interference (RFI) we expect to simultaneously observe 44+ α -transitions with sufficient sensitivity to either detect the lines or place stringent upper limits on the theoretical models of line intensity and width. At these frequencies, the CRRLs are expected to appear in emission, whereas they were observed in absorption by LOFAR. The JVLA also has sufficient angular resolution with B-configuration (maximum baseline of 11.1 km) to resolve the nuclear region of M82 separately from the rest of the galaxy, enabling us to pinpoint the spatial location of the CRRLs.

This paper outlines the JVLA P-band observations of CRRLs in M82, which are also the first spectroscopic observations performed with the JVLA’s P band. Sections 6.2 and 6.3 outline observations and data reduction, respectively. Section 6.4 describes the spectral extraction and stacking of CRRLs. Results are presented in section 6.5. Discussion and conclusions follow in section 6.6 and section 6.7, respectively.

6.2 Observations

The data were taken in several blocks as part of the Resident Shared Risk Observing (RSRO) program during semester 15A. Table 6.1 summarizes the observations, which were all performed during B-configuration with identical frequency coverage. The only exception was the test block, which was observed prior to the semester when the array was still moving from A- to B-configuration. The observational blocks were dynamically scheduled and therefore vary in length, but all start and end with a standard flux calibrator, which was interleaved throughout the observation for calibration purposes. To maximize time on source, we decided not to include a separate phase calibrator, instead using a widefield model from a reduction of the TIFR GMRT Sky Survey (TGSS; Intema et al., 2016). Block 3 includes two flux calibrators because neither of them was visible for the entire observation. In practice we used only the first calibrator, 3C 147, for the data reduction of this block.

Table 6.1: Observational summary of the data taken with the JVL A.

	Date	Calibrator	Start UTC	Duration (h)	# antennae
Test Block	2015 Jan 30	3C 147	05:35:19	1.00	27
Block 1	2015 Mar 22	3C 147	04:03:23	2.15	27
Block 2	2015 Mar 27	3C 295	07:17:27	3.65	26
Block 3	2015 Mar 29	3C 147 / 3C 295	06:18:05	4.00	25
Block 4	2015 Apr 2	3C 295	06:34:19	3.65	27
Block 5	2015 Apr 4	3C 295	06:38:33	3.15	27

We used both intermediate frequencies (IFs; A0/C0 and B0/D0) with dual polarization to cover the frequency range of 248 to 453 MHz with overlapping spectral windows to provide uninterrupted frequency coverage and optimize CRRL placement. We were limited in bandwidth by the desired channel width (7.8125 kHz , $9.44 \text{ km s}^{-1} - 5.17 \text{ km s}^{-1}$) and the total allowable data rate. We used recirculation to increase the number of channels to 4096 for seven of the spectral windows with 32 MHz bandwidth each, and 2048 channels in one spectral window covering 16 MHz bandwidth. Details of the spectral windows are listed in Table 6.2.

6.3 Data Reduction

For the data reduction we used the Common Astronomy Software Applications package (CASA). The JVLA data were downloaded in science data model/binary data format (SDM/BDF) from the NRAO archive. After importing these data into the CASA measurement set (MS) format, the online flags were applied. A gain curve was calculated to compensate for instrumental elevation effects and applied to the data. We flagged the channels containing radio frequency interference (RFI) from MUOS satellites: channels 539 through 3041 in spectral window 4, corresponding to frequencies 360.211–379.766 MHz. The unflagged data were split out and Hanning smoothed to suppress Gibbs ringing around bright RFI.

The P band contains more RFI than most JVLA bands, a more elaborate process of RFI flagging was required. To avoid manually flagging the entire dataset, we used an interactive scheme with visual inspection in between non-interactive steps. First the TFCROP algorithm was applied to blocks 1 through 5 in order to remove the strongest interference. The result was inspected for each spectral window in each block to assess the usability. Spectral window 0 in its entirety and spectral window 1 up to channel 1700 were deemed unusable due to an extreme amount of RFI. The remaining data were inspected per scan for each block and spectral window, and scans showing signs of correlation failures and other instrumental issues were discarded. Some scans were only unusable for a fraction of their duration, and we flagged only the bad time ranges. At this point the MSes were split into individual spectral windows, which were processed separately. Because the data reduction is computationally expensive, we decided to focus on spectral windows 1 and 2 for now, as there are more CRRLs per spectral window at the lower frequencies of the P band.

Ten per cent of the channels are flagged on each side of the MS due to band-pass drop-off. Initial delays and bandpass corrections were determined from

Table 6.2: Details of the spectral windows in the JVLA data and the percentage of points flagged at the end of the reduction process.

	# channels	Channel width (kHz)	Start frequency (MHz)	End frequency (MHz)	Bandwidth (MHz)	Flagging (%)
Spectral window 0	4096	7.8125	248	280	32	100.0
Spectral window 1	4096	7.8125	275	307	32	68.7
Spectral window 2	4096	7.8125	302	334	32	36.6
Spectral window 3	4096	7.8125	329	361	32	...
Spectral window 4	4096	7.8125	356	388	32	...
Spectral window 5	4096	7.8125	383	415	32	...
Spectral window 6	4096	7.8125	410	442	32	...
Spectral window 7	2048	7.8125	437	453	16	...

one manually cleaned scan of the calibrator (approximately 4 min in duration) from block 3. These initial corrections were transferred to the calibrator data in the MS, together with an initial correction for the bandpass phases. This was followed by automatic RFI flagging with PIEFLAG (Middelberg, 2006; Hales & Middelberg, 2014), a CASA task to identify and remove bad data based on the statistics of an RFI-free reference channel. Any channel that was at least 97.5 per cent flagged was removed entirely. Remaining channels or time ranges obviously affected by RFI were identified by eye and flagged. After flagging was completed, the calibrator’s delays and bandpass were redetermined. For the target, bandpass phase corrections were derived and applied together with the calibrator-derived delays and bandpass corrections. The PIEFLAG algorithm was run and remaining RFI was removed using visual inspection. At this point block 1, spectral window 1 was found to contain too many instrumentation-related problems, prompting its exclusion from further processing.

The delay- and bandpass-corrected data were subsequently split and averaged to a 16-channel MS, which is the maximum averaging that can be done while keeping bandwidth smearing negligible. Antenna gains for the calibrator were found using a point source model, appropriate for the resolution of these observations, with the Scaife–Heald (2012) standard. Phase-only calibration on the target was performed against a model derived from a 42.67 arcmin cut-out of the TGSS image, w -projected across 32 planes, using a single solution for all 16 channels. This calibration table and the calibrator’s flux scale were then transferred to the target in the 4096-channel MS.

The calibrated blocks were concatenated into one MS per spectral window, dropping completely flagged rows. The percentage of data flagged is displayed in the last column of Table 6.2. Channel cubes were made for M82 with the CLEAN algorithm, using only channels within approximately 750 km s^{-1} of each expected CRRL, using the same spatial specifications as the phase-calibration model. The cleaning mask was generated with PYBDSM (Mohan & Rafferty, 2015) from a multifrequency-synthesized image of M82 using the entire spectral window. We used a cleaning threshold of 60 mJy, which is approximately three times the RMS determined from a manually cleaned cube. Taking into account the amount of flagged data and the bandwidth used, the rms noise is 1.4 times above the expected noise. The resulting cubes, with beam sizes of about 40 by 30 arcsec, were reconvolved to 60 arcsec circular beams to spatially smooth the extracted spectra and ensure one aperture would be valid for all channels.

6.4 Extracting and Stacking the CRRLs

The cleaned channels were arranged in 1000km s^{-1} wide ‘subbands’ centred around the expected line positions. Drastic outliers were identified from a visual inspection and removed. We tested multiple extraction radii, from 1.6 to 3.0 times the standard deviation σ of a Gaussian fitted to M82’s flux.

As the CRRLs are too weak to detect individually, line stacking is required. Though M82 has a systemic optical velocity of $210 \pm 20\text{km s}^{-1}$ relative to the local standard of rest (LSR), the nuclear region alone shows velocities varying between 100 and 340km s^{-1} (Wills et al., 1998; Kepley et al., 2014). Care therefore has to be taken in selecting the proper stacking velocity, which will depend on the location of the CRRLs’ origin. We tested two different velocities: 211km s^{-1} with respect to LSR (corresponding to a redshift $z \approx 0.00073$) as found by Morabito et al. (2014), 205km s^{-1} ($z \approx 0.00068$) as found in LOFAR HBA observations of CRRLs in emission (Toribio et al., in preparation).

Before stacking, the subbands were corrected for residual bandpass effects. LOFAR HBA observations found a CRRL width of 65.8km s^{-1} FWHM in emission (M. C. Toribio, private communication). The line width in our observations is expected to be comparable. We therefore blank a region of $\pm 40\text{km s}^{-1}$ around the line centre and fit a polynomial to the remaining continuum. The polynomial order differs per subband, ranging from one through five. We divided the extracted flux by the fitted polynomial and subtracted from unity. Points more than three times the standard deviation away from zero were removed.

There were 12 lines in the unflagged parts of spectral windows 1 and 2, two of which had to be discarded because the residual bandpass was too irregular. The remaining ten lines have principle quantum numbers $n = 271$ and 273 through 282. None of the different combinations of extraction radius and systemic velocity produced a detection visible by eye. We therefore attempted to smooth the spectrum with an appropriate low-pass filter. We tested Savitzky–Golay filters (Savitzky & Golay, 1964) of orders 1 and 2, a boxcar filter, and a general least-squares filter, using filter widths from 5 to 61 points (corresponding to approximately 4 to 46km s^{-1}). The signal-to-noise ratio was approximated by dividing the standard deviation of the filtered stack within the blanking region by the standard deviation of the filtered stack outside of the blanking region. A maximum signal-to-noise ratio of 1.6 was found for a general least-squares filter with a width of 11 points, using a Gaussian aperture with a radius of 2.0σ and a redshift $z = 0.00068$. This extraction radius corresponds to an area with a physical diameter of $\sim 1.8\text{kpc}$. The stack is shown in Figure 6.1.

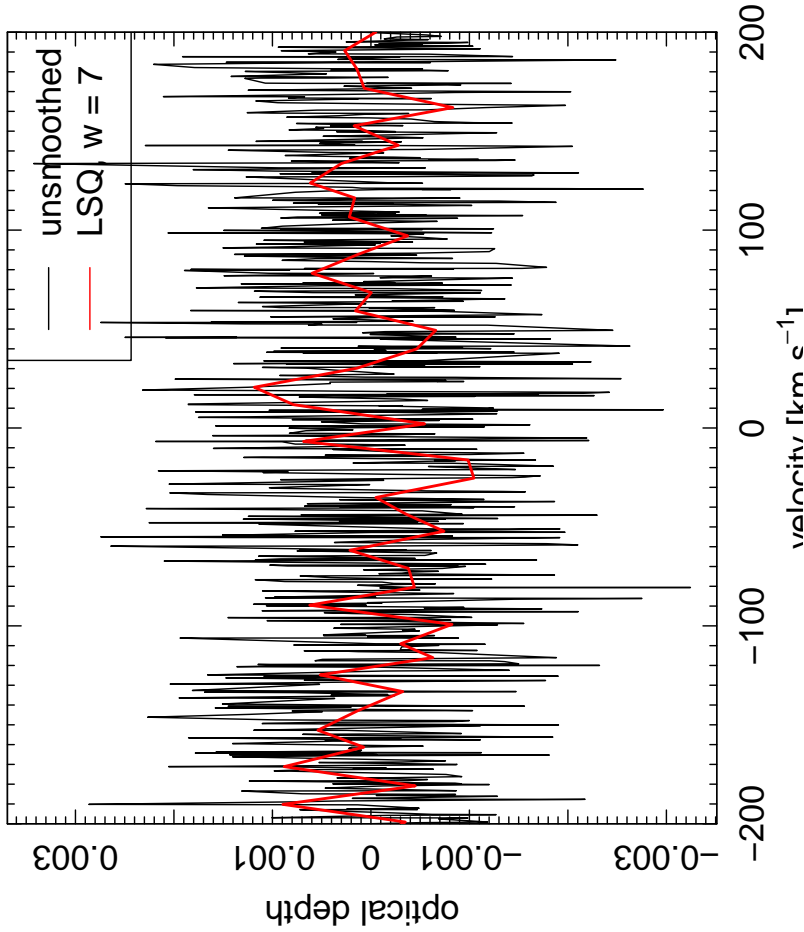


Figure 6.1: Stacked CRRL spectra from spectral windows 1 and 2, overlaid with a general least-squares filter of width 11. The subbands were stacked at redshift $z = 0.00068$, corresponding to a systematic optical velocity of 205 km s^{-1} with respect to the local standard of rest. Velocities are given in optical convention and relative to the systematic velocity. The velocity coverage in the central $\pm 200 \text{ km s}^{-1}$ is $\sim 0.75 \text{ km s}^{-1}$ per point. There is no detection of the CRRLs. The root-mean-square optical depth of the central $\pm 40 \text{ km s}^{-1}$ is 1.4×10^{-3} .

6.5 Results

As the signal-to-noise ratio of the best stack is too low for a detection, we determine an upper limit to the peak optical depth by calculating the root-mean-square of the best stack in the central $\pm 40 \text{ km s}^{-1}$. This upper limit is $\tau_{\text{peak}} < 1.4 \times 10^{-3}$. Assuming a FWHM of 65.8 km s^{-1} , the corresponding lower limit on the integrated optical depth is $\tau_{\text{int}} > -100 \text{ Hz}$. We adopt a ten per cent uncertainty on this value to account for the possibility of a different FWHM, resulting in $\tau_{\text{int}} = -100^{+100}_{-10} \text{ Hz}$.

This result, together with previously determined integrated optical depths from LOFAR LBA ($\tau_{\text{int}} = 21.3^{+1}_{-5} \text{ Hz}$, Morabito et al., 2014) and HBA ($\tau_{\text{int}} = -30 \pm 2 \text{ Hz}$, M. C. Toribio, private communication) observations, can be used to constrain the electron temperature and density of the cold neutral medium in M82. Detailed theoretical models of CRRLs (F. Salgado et al., submitted) predict the departure from local thermal equilibrium (LTE), which can be converted into integrated optical depth, for given values of the electron temperature T_e and electron density n_e . Modelled departure coefficients, defined as the ratio between actual and LTE level populations, were calculated for a grid of values for these two parameters. T_e varied from 10 to 250 K in steps of 5 K. The density n_e varied from 0.01 to 0.110 cm^{-3} in steps of 0.005 cm^{-3} . We assume the background radiation temperature follows the Galactic power law

$$T_R = T_0 \left(\frac{\nu}{\nu_0} \right)^{-2.6}, \quad (6.1)$$

with reference temperature $T_0 = 2000 \text{ K}$ at $\nu_0 = 100 \text{ MHz}$. This is based on Galactic values, which were estimated from the radio continuum at 408 MHz (Haslam et al., 1982). We estimated the radiation temperature of the nuclear region from previous higher-resolution HBA observations to be $\sim 3000 \text{ K}$. Thus $T_0 = 2000 \text{ K}$ is a reasonable assumption.

To scale the departure coefficients to integrated optical depth, the emission measure, defined as

$$\text{EM} = \int_0^L n_{\text{CII}} n_e ds, \quad (6.2)$$

where the ds is a path element along the line of sight, is required. We assume that in the otherwise neutral medium, all electrons come from singly ionised carbon. If the carbon population is mostly in C II then $n_e \approx n_{\text{CII}}$. If the electron density is constant along the line of sight, or if it is appropriately averaged, the

emission measure simplifies to

$$\text{EM} = n_e^2 L, \quad (6.3)$$

where $L \equiv \int ds$ is the path length through the observed object.

Because we only have two optical depth measurements and one lower limit, an assumption for L has to be made for the comparison of the model to the observations to be well constrained. Welichew et al. (1984) found that the H I distribution in M82 can be described as a toroid with an inner radius of 170 ± 20 pc and an outer radius of 340 ± 30 pc. Assuming that the CRRLs trace the cold H I, a line of sight through the centre of the toroid, from end to end, corresponds to a path length of 340 pc. We assume that the detected CRRLs in emission originate from clouds distributed throughout the toroid, therefore we adopt $L = 340$ pc in this case (unity filling factor).

For the CRRLs in absorption we test two different assumptions. The simplest assumption is that the path length will be the same for both emission and absorption. However, one could also argue that if the absorbed emission originates from M82's nucleus only the clouds in front of the nucleus can be the origin of the CRRLs in absorption, and that therefore the path length for absorption should be 170 pc. Evidence for this is found in the HBA detection of CRRLs, which have a centroid offset from that of the LBA detection by -15.8 km s^{-1} , and a wider full width half maximum. The larger line width in emission could be explained by a line of sight through a larger number of independently moving clouds of H I.

Chi-squared values are calculated by comparing the models in this grid with the observed integrated optical depths. Confidence intervals on the grid were determined by integrating $1/\chi^2(T_e, n_e)$ over the grid, starting at the highest value of $1/\chi^2$ and including progressively lower values until the integrated volume encompasses a 1σ , 2σ , or 3σ fraction of the total volume. The resulting confidence intervals are shown in Figure 6.2.

To obtain separate constraints on T_e and n_e , we collapsed the grids along these two axes and integrated outwards from the maximum value to determine one-dimensional confidence intervals and the values with maximum $1/\chi^2$. For the case where $L = 340$ pc for both emission and absorption, we determined $T_e = 95_{-85}^{+105}$ K and $n_e = 0.030 \pm 0.005 \text{ cm}^{-3}$, where the errors are based on the 1σ one-dimensional confidence intervals. If we assumed the path length is 340 pc for emission and 170 pc for absorption, the result was $T_e = 85_{-75}^{+100}$ K and $n_e = 0.04 \pm 0.005 \text{ cm}^{-3}$. The best fit models are shown in Fig. 6.3. Both cases describe the data well; to judge which assumption on the path length is more correct a

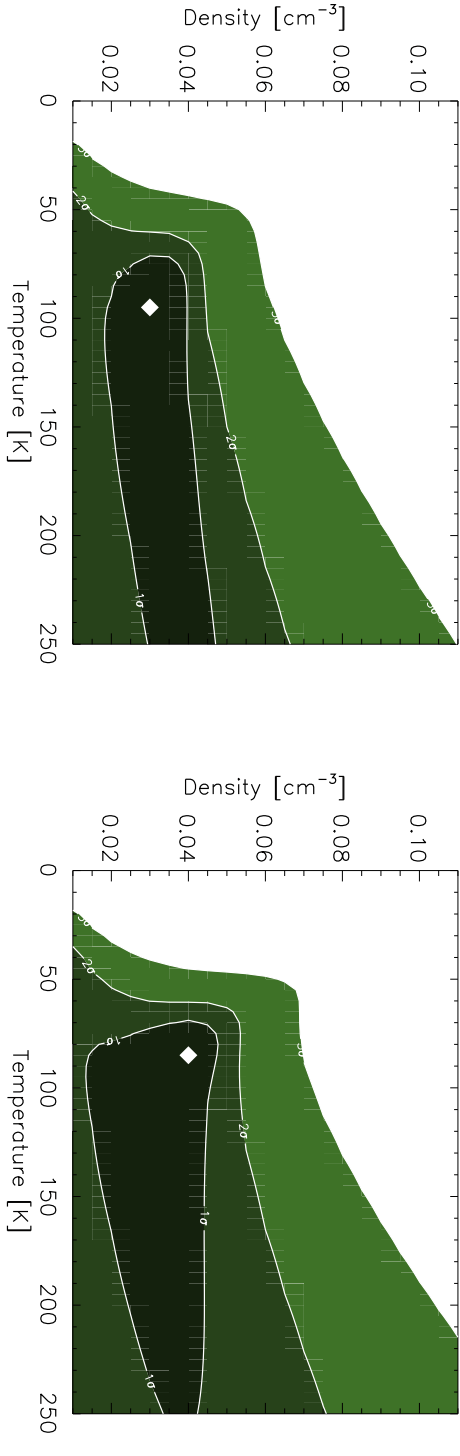


Figure 6.2: Confidence intervals on the electron temperature T_e and electron density n_e based on the observed and modelled integrated optical depths. In the left panel it is assumed that the path length is 340 pc for both emission and absorption, while in the right panel the path length is 340 pc for emission and 170 pc for absorption. The three regions are 1σ , 2σ , and 3σ confidence intervals, from the darkest to the lightest shade. The best-fit value is indicated by a white diamond.

Figure 6.3: Integrated optical depths plotted with the two best-fit models. The solid blue line is for the best fit model with a single path length of 340 pc. The dashed blue line is for the best fit model assuming a path length of 340 pc for emission and 170 pc for absorption.

stricter lower limit on the integrated optical depth or a detection of the CRRLs in the P band is required. In the following we base our calculations on the case that $L = 340\text{pc}$ in both emission and absorption, as it is the simpler assumption of the two. Because the results above are in agreement with each other, the following calculations will not change significantly if we choose the other set of results.

6.6 Discussion

The values found for T_e and n_e are compatible with the expectation that we observe diffuse CRRLs that trace the CNM. Morabito et al. (2014) found that the CRRLs in M82 are likely associated with the neutral hydrogen in M82, which is also seen in our own Galaxy (e.g., Anantharamaiah et al., 1994). The values of T_e and n_e from this paper are also similar to Galactic values. For example, Oonk et al. (2014) found values of $T_e \sim 110\text{K}$ and $n_e \sim 0.06\text{cm}^{-3}$ in the direction of bright background source Cygnus A. This is supporting evidence that CRRLs in our Galaxy and in M82 originate in similar conditions.

If we assume that the CRRLs trace the cold H I gas component in M82, the free electrons should be supplied by carbon, and $n_e \approx n_C$. The path length L can be used to convert density (cm^{-3}) to column density (cm^{-2}) for a comparison with previously measured H I column densities. This provides an estimation of the carbon-to-hydrogen ratio. For $L = 340\text{pc}$, the column density is $N_{\text{CII}} \sim 3.2 \pm 0.5 \times 10^{19}\text{cm}^{-2}$. Measured column densities for cold H I in the direction of supernovae remnants in the nuclear region of M82 range from $> 30 \times 10^{21}$ to $< 1.6 \times 10^{21}\text{cm}^{-2}$ (Wills et al., 1998). The ratio C II/H I therefore ranges from 1.1×10^{-3} to 2.0×10^{-2} .

The estimated C II/H I ratio is about an order of magnitude higher than what has previously been measured for the diffuse interstellar medium (1.4×10^{-4} ; Sofia et al., 1997). It is likely that our estimated ratio is actually higher than the real value, as the H I column density measurements are from observations with small beams that do not cover the entire region from which CRRLs may originate, and there is a tendency for higher column densities to be associated with the supernovae remnants unaffected by free-free absorption (thought to be associated with the LBA CRRL; see Morabito et al., 2014). The relevant H I content in the CNM may therefore be underestimated. This would decrease the upper limit on the C II/H I ratio. The ratio would also be reduced if the C II column density is actually smaller than the upper limit quoted here. It is difficult to estimate how this would change, as L , T_e , and n_e are degenerate and changes in path length and/or density could be absorbed by changes in T_e . Spatially resolving the region of CRRL emission is necessary to further constrain the path

length, and more measurements spread in frequency will help further constrain the temperature and density. It is not unreasonable to expect a higher C II/H I ratio in M82, as carbon enhancement associated with the nuclear region has been observed (e.g., White et al., 1994).

We can derive a total mass for C II using n_e and the Carbon mass density, $\rho_C = (6.0 \pm 4.0) \times 10^{-25} \text{ g cm}^{-3}$, and assuming that the C II gas comes from a volume equal to that of the toroid described by (Weliachew et al., 1984). The volume of this toroid is on the order of $(2 - 3) \times 10^7 \text{ pc}^3$, we therefore find a total carbon mass of $M_{\text{CII}} \sim (1 - 3) \times 10^5 M_\odot$. Assuming that the CNM mass is dominated by H I and C II, its total mass is:

$$M_{\text{CNM}} \approx \left(1 + \frac{m_{\text{H}}}{m_{\text{C}}} \left[\frac{\text{H}}{\text{CII}} \right] \right) M_{\text{CII}}. \quad (6.4)$$

For C II/H I $\sim 2.0 \times 10^{-2}$, this provides $M_{\text{CNM}} \sim 5.3 \times 10^5 - 1.6 \times 10^6 M_\odot$. For C II/H I $\sim 1.1 \times 10^{-3}$ the mass ranges from $M_{\text{CNM}} \sim 8.1 \times 10^6 - 2.4 \times 10^7 M_\odot$. Weliachew et al. (1984) estimated $M_{\text{HI}} \sim 1.2 \times 10^7 M_\odot$, which is in agreement with the masses calculated for the smaller C II/H I ratio of $\sim 1.1 \times 10^{-3}$. The total CNM mass estimates are $\sim 0.2 - 14$ per cent of the dense molecular gas mass in M82's nucleus, which is $M_{\text{dense}} \sim (1.7 - 2.7) \times 10^8 M_\odot$ (Naylor et al., 2010).

6.7 Conclusions

We have analysed spectroscopic observations of M82 with the JVL A P band to study diffuse CRRLs. By stacking 10 CRRL α -transitions, we provided an upper limit of 1.4×10^{-3} on the peak optical depth and a lower limit of -100 Hz on the integrated optical depth. Comparing the lower limit on the integrated optical depth with a grid of detailed theoretical models of low-frequency CRRLs allowed us to constrain the electron density and temperature to $T_e = 95_{-85}^{+105} \text{ K}$ and $n_e = 0.030 \pm 0.005 \text{ cm}^{-3}$. These values are similar to what has been seen for the CNM in our own Galaxy. By using the assumed path length $L = 340 \text{ pc}$ for the H I distribution as measured by Weliachew et al. (1984), we estimate a total C II column density of $3.2 \pm 0.5 \times 10^{19} \text{ cm}^{-2}$. Comparison with the range of H I column densities measured by Wills et al. (1998) therefore imply carbon-to-hydrogen ratios of $1.1 \times 10^{-3} - 2.0 \times 10^{-2}$. Using the smaller carbon to hydrogen ratio and the carbon mass density, we estimate that the CNM in M82 has a total mass of $8.1 \times 10^6 - 2.4 \times 10^7 M_\odot$, in agreement with previous measurements of the total mass of H I.

Stricter constraints on the integrated optical depth in the P band, or ideally a detection, are required to further constrain the determined T_e and n_e and test the assumptions on the path length. The work presented here only reports on 10 of the available lines, and adding more CRRL transitions would increase the signal to noise ratio by a factor of \sqrt{N} . Using conservative estimates on loss of data due to RFI flagging there will be a minimum of 20 lines available for stacking. By using these CRRL transitions we will increase the signal to noise and provide either tighter limits on or a detection of the CRRLs.

Acknowledgements

SLZ and JBRO acknowledge financial support from NWO Top LOFAR-CRRL project, project n. 614.001.351. LKM acknowledges financial support from NWO Top LOFAR project, project n. 614.001.006.

Bibliography

- Adebahr B., Krause M., Klein U., Weżgowiec M., Bomans D. J., Dettmar R.-J., 2013, *A&A*, 555, A23
- Anantharamaiah K. R., Erickson W. C., Payne H. E., Kantharia N. G., 1994, *ApJ*, 430, 682
- Brocklehurst M., Seaton M. J., 1972, *MNRAS*, 157, 179
- Fenech D., Beswick R., Muxlow T. W. B., Pedlar A., Argo M. K., 2010, *MNRAS*, 408, 607
- Gandhi P., Isobe N., Birkinshaw M., Worrall D. M., Sakon I., Iwasawa K., Bamba A., 2011, *PASJ*, 63, 505
- Hales C. A., Middelberg E., 2014, *Astrophysics Source Code Library*, record ascl:1408.014
- Haslam C. G. T., Salter C. J., Stoffel H., Wilson W. E., 1982, *AAPS*, 47, 1
- Intema H. T., Jagannathan P., Mooley K. P., Frail D. A., 2016, preprint, ([arXiv:1603.04368](https://arxiv.org/abs/1603.04368))
- Kepley A. A., Leroy A. K., Frayer D., Usero A., Marvil J., Walter F., 2014, *ApJL*, 780, L13
- Lo K. Y., Cheung K. W., Masson C. R., Phillips T. G., Scott S. L., Woody D. P., 1987, *ApJ*, 312, 574
- McDonald A. R., Muxlow T. W. B., Wills K. A., Pedlar A., Beswick R. J., 2002, *MNRAS*, 334, 912
- Middelberg E., 2006, *PASA*, 2, 64
- Mohan N., Rafferty D., 2015, *Astrophysics Source Code Library*, record ascl:1502.007
- Morabito L. K., et al., 2014, *ApJL*, 795, L33
- Muxlow T. W. B., Pedlar A., Wilkinson P. N., Axon D. J., Sanders E. M., de Bruyn A. G., 1994, *MNRAS*, 266, 455
- Naylor B. J., et al., 2010, *ApJ*, 722, 668
- Oonk J. B. R., et al., 2014, *MNRAS*, 437, 3506

- Perley R. A., Chandler C. J., Butler B. J., Wrobel J. M., 2011, *ApJL*, 739, L1
- Ponomarev V. O., Sorochenko R. L., 1992, *Soviet Astronomy Letters*, 18, 215
- Savitzky A., Golay M. J. E., 1964, *Analytical Chemistry*, 36, 1627
- Scaife A. M. M., Heald G. H., 2012, *MNRAS*, 423, L30
- Sofia U. J., Cardelli J. A., Guerin K. P., Meyer D. M., 1997, *ApJL*, 482, L105
- Walmsley C. M., Watson W. D., 1982, *ApJ*, 260, 317
- Weliachew L., Fomalont E. B., Greisen E. W., 1984, *A&A*, 137, 335
- White G. J., Ellison B., Claude S., Dent W. R. F., Matheson D. N., 1994, *A&A*, 284, L23
- Wills K. A., Pedlar A., Muxlow T. W. B., Wilkinson P. N., 1997, *MNRAS*, 291, 517
- Wills K. A., Pedlar A., Muxlow T. W. B., 1998, *MNRAS*, 298, 347
- Yun M. S., Ho P. T. P., Lo K. Y., 1993, *ApJL*, 411, L17
- van Haarlem M. P., et al., 2013, *A&A*, 556, A2